Mesoscopic Field-Effect-Induced Devices in Depleted Two-Dimensional Electron Systems

N. Bachsoliani,[1] S. Platonov,[1,2] A. D. Wieck,[3] and S. Ludwig[2]
[1]*Center for NanoScience and Fakultät für Physik, Ludwig-Maximilians-Universität, Schellingstraße 4, 80799 München, Germany*
[2]*Paul-Drude-Institut für Festkörperelektronik, Leibniz-Institut im Forschungsverbund Berlin e.V., Hausvogteiplatz 5–7, 10117 Berlin, Germany*
[3]*Angewandte Festkörperphysik, Ruhr-Universität Bochum, Universitätsstrasse 150, 44780 Bochum, Germany*
(Received 8 August 2017; revised manuscript received 20 November 2017; published 14 December 2017)

Nanoelectronic devices embedded in the two-dimensional electron system (2DES) of a GaAs/(Al, Ga)As heterostructure enable a large variety of applications ranging from fundamental research to high-speed transistors. Electrical circuits are thereby commonly defined by creating barriers for carriers by the selective depletion of a preexisting 2DES. We explore an alternative approach: we deplete the 2DES globally by applying a negative voltage to a global top gate and screen the electric field of the top gate only locally using nanoscale gates placed on the wafer surface between the plane of the 2DES and the top gate. Free carriers are located beneath the screen gates, and their properties can be controlled by means of geometry and applied voltages. This method promises considerable advantages for the definition of complex circuits by the electric-field effect, as it allows us to reduce the number of gates and simplify gate geometries. Examples are carrier systems with ring topology or large arrays of quantum dots. We present a first exploration of this method pursuing field effect, Hall effect, and Aharonov-Bohm measurements to study electrostatic, dynamic, and coherent properties.

DOI: 10.1103/PhysRevApplied.8.064015

I. INTRODUCTION

The electric-field effect is a powerful tool for nanoelectronics. It is widely used for creating potential barriers in a two-dimensional electron system (2DES) by applying voltages to individual metal gates placed on the wafer surface. When used with multiple individual gates, it provides full tunability while also being compatible with high-mobility wafers. Alternative methods for structuring a 2DES include etching [1–4] and surface oxidation techniques [5,6]. While they ensure additional possibilities in combination with in-plane side gates [7] or metal gates [8,9], etching and oxidation techniques alone lack tunability. More importantly, they are restricted to wafers with a shallow 2DES causing a close proximity of surface states and doping atoms limiting the carrier mobility [10] and the electrostatic stability at the nanoscale (related to the $1/f$ spectrum of charge noise [11–13]). Applications based on the quantum-mechanical coherence of localized carriers require superior control and stability favoring the field effect.

A straightforward—and the most common—approach to shaping potential landscapes by the field effect, starting from an extended 2DES, is based on the controlled local depletion of the 2DES beneath individual surface gates. This approach works perfectly for relatively small structures with a simple topology, such as few-coupled quantum dots [14,15] or quantum point contacts. However, an individually tunable one-dimensional array of N quantum dots requires at least about $2N$ metal gates, while even more gates are needed for a two-dimensional array or for increased tunability. Failure of a single gate would alter the current path and typically make the entire device useless. Furthermore, nontrivial topologies, such as an Aharonov-Bohm ring allowing carriers to move in a circle around a depleted center, require voltage biasing of a center gate without depleting the surrounding carriers. This goal has been achieved by implementation of three-dimensional air bridges [16,17]. However, the fabrication of air bridges is rather complex and is limited to relatively big structures.

In this article, we propose an alternative method to define complex nanoelectronic circuits based on the field effect, offering full tunability of high-quality devices. Compared to common strategies, our method simplifies the production of ring topologies and offers the prospect of scalability while limiting the danger of general failure. Our idea, sketched in Fig. 1(a), is based on globally depleting the 2DES using a single top gate while we place nanoscale screen gates between the top gate and the 2DES to locally shield the effect of the top gate and thereby regain free carriers. We electrically isolate the top gate from the screen gates using an approximately 100-nm-thick layer of cross-linked PMMA [18,19], while the 2DES at the interface between (Al,Ga)As and GaAs is separate from the screen gates on the wafer surface by another 110 nm, consisting of the following electrically insulating layers: a 5-nm-thick capping layer of GaAs to prevent oxidation of the surface, followed by 70 nm of homogeneously

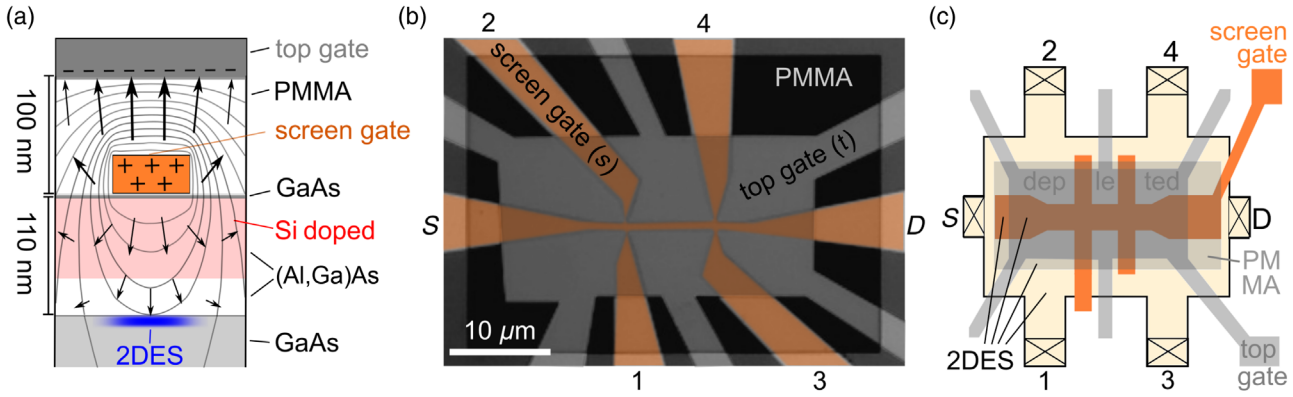

FIG. 1. (a) Sketch of the heterostructure with screen and top gates. The top gate (gray) is biased at $V_t = -1$ V and the screen gate at $V_s = 0.1$ V, and the 2DES (blue) is grounded. Away from the screen gate but below the top gate, the 2DES is absent (fully depleted). The electrostatic potential (shown as equally spaced equipotential lines; arrows indicate the field strength) has been calculated by self-consistently solving the Poisson equation using $\epsilon = 2$ for cross-linked PMMA and $\epsilon = 12.7$ for (Al,Ga)As. For the calculation, we consider charges on the gates and in the 2DES but neglect the effect of positively charged doping ions which are immobile at cryogenic temperatures. (b) False-colored optical microscope image of a Hall-bar sample. Orange indicates the screen gate (s) covered by cross-linked PMMA (dark) and, finally, the top gate (gray). (c) Descriptive sketch of the sample surface. As in (b), it shows the screen gate (orange) covered by PMMA (light gray, slightly yellow) and the top gate (gray). At the white surrounding the sample, the surface is etched away such that the 2DES is destroyed. Ohmic contacts to the 2DES for source (S), drain (D), and voltage probes (1, 2, 3, 4) are indicated by crosses. In a Hall-bar measurement, the 2DES is depleted beneath the top gate but not beneath the screen gate. Yellow regions are not covered by a gate and always contain a conducting 2DES 110 nm beneath the surface.

Si-doped $Al_{0.36}Ga_{0.64}As$, and 35 nm of undoped $Al_{0.36}Ga_{0.64}As$ [20,21]. The carrier density and the detailed geometry of the confinement potential depend on the electric field at the 2DES and can be fine-tuned by adjusting the voltages applied to both the top gate and the screen gate. In Fig. 1(a), we sketch the screening effect on a grounded 2DES for the example of a positively charged screen gate beneath a negatively charged top gate. A global top gate above gates at the surface has been used before for different purposes. In a previous attempt to structure a 2DES, a single top gate was combined with a local dielectric to partially screen the field of the global top gate [22,23]. Here, the missing screen gate results in a reduced tunability compared to our approach. A global top gate has also been employed to decrease telegraph noise [12] or to incorporate carriers in undoped quantum wells [24,25]. In the last two examples, gates on the GaAs surface are used to locally deplete the 2DES, while, in our case, carriers accumulate beneath the screen gate.

In Fig. 1(b), we display a SEM image of an actual Hall-bar sample, and in Fig. 1(c) a descriptive sketch. The screen gate (s) directly on the sample surface is shown in orange, the top gate (t) above, which is electrically isolated by cross-linked PMMA, in light gray. By charging the top gate negatively with respect to the grounded 2DES and a grounded back gate at the bottom of the 540-μm-thick wafer, we deplete the 2DES beneath the top gate wherever it is not shielded by the screen gate. Below the top gate, the shape of the screen gate corresponds to the approximate shape of the 2DES beneath. The screen gate in Fig. 1(b) defines a Hall bar with source (S) and drain (D) for the current and four side contacts used as voltage probes (1, 2, 3, 4). The top gate includes a large center square and six arms reaching to the outside. The arms have the function to avoid electrical shorts between the six contacts outside of the Hall-bar region where they would otherwise be shorted by 2DES [as the yellow areas in Fig. 1(c) are conducting].

In our Hall bar, the free carriers are located directly beneath a metal gate, which results in two important differences from traditional devices: the direct vicinity of metal can reduce the disorder potential, as charged defects are partly screened by electron rearrangement at the metal surface. At the same time, the metal will tend to screen the electron-electron interaction in the 2DES below. In this article, we do not explore this reduced Coulomb interaction but rather demonstrate the general feasibility of our method.

II. FIELD-EFFECT CHARACTERIZATION

For a first characterization of our device, we present in Fig. 2 the current flowing between source and drain contacts (while the side contacts are left floating) in response to a source-drain voltage of $V_{SD} = 0.84$ mV as a function of both the top-gate and screen-gate voltages, V_t and V_s. The lines of constant current display a kink at $V_t \equiv V_t^d = -1.48$ V, marked by a dashed horizontal line in Figs. 2(a) and 2(b), indicating complete depletion of the 2DES for $V_t < V_t^d$. The almost-constant slope of each line of constant current for $V_t < V_t^d$ suggests, for a given value of V_s, a constant ratio of the capacitances between the Hall bar and the two respective gates, $C_s/C_t = dV_t/dV_s$. To keep the current constant, a change in the screen-gate

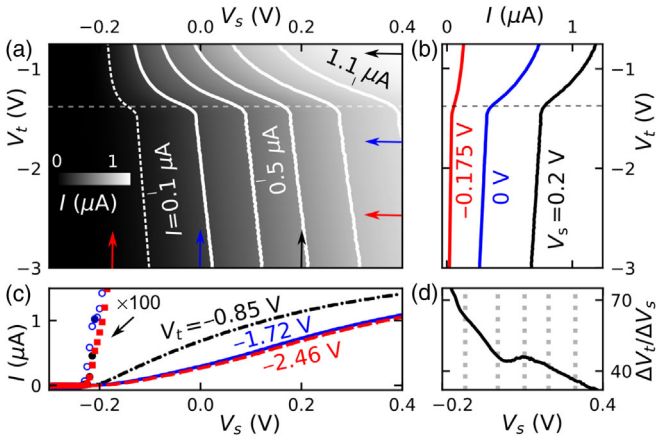

FIG. 2. (a) Current I through the Hall bar at $V_{SD} = 0.84$ mV (gray scale and lines of constant current at an interval of 0.2 μV) as a function of the top gate V_t (y-axis) and screen gate V_s (x-axis) voltages. The horizontal dashed line at $V_t \equiv V_t^d = -1.48$ V indicates the onset of depletion of the 2DES below the top gate away from the screen gate. (b),(c) Vertical and horizontal cuts $I(V_t)$ and $I(V_s)$ from (a) (fixed voltages V_s and V_t, respectively, are indicated by color-coded arrows). Symbols in (c) represent identical data multiplied by a factor of 100 to demonstrate complete pinch-off for $V_s < -0.228$ V, independent of V_t. (d) The slope dV_t/dV_s of the constant current lines versus V_s at $V_t = -2.5$ V. Vertical dashed lines indicate intersections with the constant current lines in (a).

voltage by δV_s can be compensated for by a shift of the top-gate voltage by $\delta V_t = -\delta V_s C_s/C_t$. The value of C_s/C_t quantifies the shielding of the influence of the top gate on the 2DES by the screen gate. It depends on the dielectric constants and geometry of the layers, which influence the electric field originating from the top gate. The coupling ratio, which we plot in Fig. 2(d) versus V_s, takes the large value of $C_s/C_t \simeq 75$ at $V_s \simeq -200$ mV near depletion, where it indicates an efficient screening of the top gate by the screen gate. The gradual increase to $C_s/C_t \simeq 45$ at $V_s \simeq 300$ mV indicates a growing influence of the top gate at a more positive V_s. Because the 2DES shaping the Hall bar is the only variable component of our system, the observed reduction of the shielding effect, as V_s is increased, indicates an increase of the Hall-bar width. Variations in the Hall-bar width, in turn, result in a rearrangement of the confinement potential perpendicular to the Hall-bar edges. Consequently, the combination of top- and screen-gate voltages can be used to tune the steepness of the confinement at the Hall-bar edges which influence the shape and stability of quantum Hall edge states [26]. Reliable predictions can be achieved by employing a Poisson-Schrödinger solver such as NEXTNANO^3 [27], while breakdown measurements of the quantum Hall effect would provide an experimental test [26]. Both ideas go beyond the scope of this paper but are topics for the future.

To quantitatively evaluate the shielding, we compare the measured capacitance ratio C_s/C_t with the ratio expected without screening, C_s/C_t^0, where C_t^0 denotes the capacitance between the top gate and the 2DES without the existence of a screen gate. For a first estimate, we compare the measured depletion voltages of the respective gates, $C_s/C_t^0 \simeq V_t^d/V_s^d \simeq 1.48/0.23 \simeq 6.4$. As a result, we find $C_t^0/C_t = (C_s/C_t)/(C_s/C_t^0) \simeq 75/6.4 \simeq 11.7$ at $V_s = -0.23$ V; i.e., the screen gate reduces the coupling of the top gate to the 2DES by roughly 1 order of magnitude. Clearly, this result depends on the geometry details and the applied voltages. The accuracy of the above numbers is around 10%, reflecting the accuracy in determining the pinch-off voltages.

In a second approach, we compare our first estimate based on direct measurements with the prediction of a simple plate-capacitor model, assuming two separate plate capacitors, one between the top gate and the 2DES—but without the screen gate—and the other between the screen gate and the 2DES. The model predicts $C_s/C_t^0 \simeq 1 + \epsilon_{(\mathrm{Al,Ga})\mathrm{As}}/d_{(\mathrm{Al,Ga})\mathrm{As}} \times d_{\mathrm{PMMA}}/\epsilon_{\mathrm{PMMA}}$, where the capacitor between the top gate and the 2DES contains two layers of dielectricum, $d_{\mathrm{PMMA}} = 100$ nm of PMMA, and $d_{(\mathrm{Al,Ga})\mathrm{As}} = 110$ nm of (Al,Ga)As. We determine the required dielectric constant of our cross-linked PMMA from our measured depletion voltage $V_t^d = -1.48$ V of the top gate and the carrier density of the 2DES $n_s^0 \simeq 1.45 \times 10^{11}$ cm^{-2} at grounded gates, $V_t = V_s = 0$, based on Hall measurements. Using our simple plate-capacitor model, we find $n_s = (d_{\mathrm{PMMA}}/\epsilon_{\mathrm{PMMA}} + d_{(\mathrm{Al,Ga})\mathrm{As}}/\epsilon_{(\mathrm{Al,Ga})\mathrm{As}})\, V_t^d/\epsilon_0$, with ϵ_0 being the vacuum permeability. Using the literature value $\epsilon_{(\mathrm{Al,Ga})\mathrm{As}} = 12.7$ [28], we find $\epsilon_{\mathrm{PMMA}} \simeq 2.0$. Finally, our plate-capacitor model predicts $C_s/C_t^0 \simeq 1 + \epsilon_{(\mathrm{Al,Ga})\mathrm{As}}/d_{(\mathrm{Al,Ga})\mathrm{As}} \times d_{\mathrm{PMMA}}/\epsilon_{\mathrm{PMMA}} \simeq 6.8$, which is in fair agreement with our first estimate. From the equation above, it is evident that a thicker insulator layer between the screen gate and the top gate with a smaller dielectric constant would increase the screening effect.

III. HALL MEASUREMENTS: CARRIER DENSITY AND MOBILITY

We aim at evaluating the quality of the 2DES in nanocircuits created with our method. Below, we use an Aharonov-Bohm ring for phase-coherent measurements. However, first we measure carrier density and mobility based on the Hall bar introduced above. As a reference, we use the "nominal" mobility and carrier density averaged over the wafer, which we measure directly after growth at the cryogenic temperature of $T = 4$, 2 K [21]. They are $\mu = 0.7 \times 10^6$ cm^2 V^{-1} s^{-1} and $n_s = 2.27 \times 10^{11}$ cm^{-2}, corresponding to a mean free path of $l_m = 5.5$ μm. In our sample, we determine the carrier density (averaged over the width of the Hall bar) by measuring the classical Hall voltage $V_H \propto 1/n_s$ and the mobility by measuring the longitudinal resistance in the limit $B \to 0$ [$R_{13} = R_{24} \propto \rho_0 \propto (n_s\mu)^{-1}$], both at $T \simeq 4.2$ K. In Fig. 3, we present our results as a function of screen-gate voltage V_s

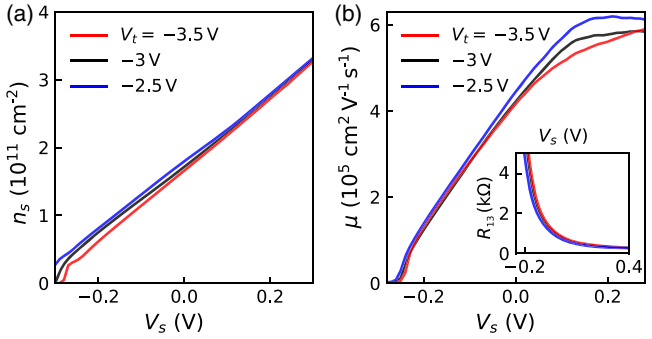

FIG. 3. Hall measurements. (a) Electron carrier density n_s and (b) mobility μ of the 2DES versus the screen-gate voltage V_s for various top-gate voltages, $V_t < V_t^d$. (Inset) The actual measured longitudinal resistance $R_{13}(V_s)$ at $B \to 0$ mT.

and for various top-gate voltages, $V_t < V_t^d$, i.e., where the 2DES beyond the Hall bar is fully depleted and the Hall bar is well defined. Both the carrier density and the mobility depend only a little on the top-gate voltage, but they are widely tunable by varying the screen-gate voltage. For $V_s < 100$ mV, we observe a linear decrease of both n_s and μ, with a decreasing V_s indicating an approximately constant capacitance C_s between 2DES and the screen gate and a resistivity $\rho_0 \propto n_s^{-2}$ (equivalent to $\mu \propto n_s$). We note that gate-voltage-independent capacitances (as our C_s value) between gates and the 2DES are not guaranteed, as this property depends on the wafer material.

In our sample, at $V_s = 0$, carrier density and mobility are reduced by approximately a factor of 2 compared to the nominal values of the pristine wafer. However, the nominal values can be recovered by applying a positive V_s value. This result suggests that wafers with a higher doping level could be advantageous for applications requiring a high mobility or a highly tunable carrier density.

IV. AHARONOV-BOHM MEASUREMENTS: PHASE COHERENCE

Our method offers a straightforward way to fabricate conducting pathways with a ring topology. In Fig. 4, we present a photography of a sample containing seven quasi-one-dimensional Aharonov-Bohm (AB) rings of various sizes and shapes in a parallel configuration connected to two-dimensional leads. The conductance of an individual ring can be measured by depleting the 2DES below the top gate and below all ring-shaped screen gates besides the one of the AB ring of interest. To explore the phase coherence of the carriers, we here concentrate on the smallest ring (rightmost in Fig. 4), which is also presented as a scanning-electron-microscope picture in Fig. 5(b). In Fig. 5(a), we present an example of AB oscillations, measured in a dilution refrigerator at a lattice temperature of 25 mK. Plotted is the current I flowing through our ring in response to a source-drain voltage of $V = 0.1$ mV versus the

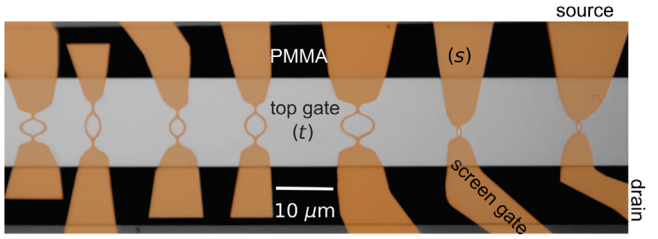

FIG. 4. False-colored optical microscope image of the Aharonov-Bohm sample with seven individual AB rings. The screen gates are depicted in orange and the top gate in gray. Unused AB rings are depleted by applying a sufficiently negative V_s value.

perpendicular magnetic field B. The AB oscillations can be formally described as

$$I = \bar{I}\left[1 + v\cos\left(\frac{e}{\hbar}AB + \delta\varphi_{\rm es}\right)\right], \qquad (1)$$

where $\bar{I}$ is the current averaged over B, $v = I_0/\bar{I}$ the visibility of the AB oscillations with amplitude I_0, and A the area enclosed by the AB ring (which weakly depends on V_s). The first term contained in the cosine is 2π times the number of enclosed magnetic flux quanta, while $\delta\varphi_{\rm es}$ sums up all other phase shifts which can be related to the existence of multiple paths (as for universal conductance fluctuations [29–31]) or geometry (such as the electrostatic AB effect [32]). The measured period of the AB oscillation in Fig. 5(a) of $\delta B \simeq 7.9$ mT corresponds to the enclosed area of $A = h/eB \simeq 0.5$ μm^2, coinciding with the area framed by the dashed line in Fig. 5(b).

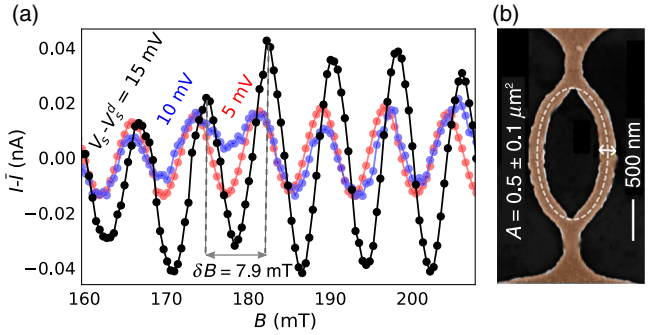

FIG. 5. (a) Measured current $I - \bar{I}$ as a function of the perpendicular magnetic field B for three values of $V_s - V_s^d$ near depletion and $V_t = -3$ V. (At V_s^d, the carriers beneath the screen gate are depleted.) The bath temperature is $T = 25$ mK and the source-drain voltage $V = 0.1$ mV. (b) Scanning-electron-microscope image of the measured AB ring. The screen gate is shown in orange. The dashed white line embraces the area of $A = 0.5$ μm^2 corresponding to the measured magnetic-field period of $\delta B = 7.9$ mT; see the text. The white double arrow indicates an error in A of ± 0.1 μm^2 corresponding to a maximum error in δB of ± 1.5 mT. This value reflects the experimental uncertainty in the tilt angle between the 2DES and the magnetic field of $\pm 1°$ (B is the field component perpendicular to the 2DES).

In order to observe the AB oscillations shown in Fig. 5(a), it is necessary to almost completely deplete the carriers in the AB ring by applying V_s close to the depletion voltage V_s^d. This observation hints at a channel width so wide that it allows for multiple paths (in each arm) contributing with individual phases to the conductance which effectively reduces the visibility of the AB oscillations [33]. As a rule of thumb, for our geometry, an enclosed area difference of about 1% would suffice to generate a phase shift of π at $B \simeq 200$ mT. The almost-depleted ring sufficiently reduces the number of possible paths to reach a visibility of a few percent. Taking the Hall-bar measurements above as a reference for the applied gate voltages, we expect a carrier density of approximately 8×10^9 cm^{-2} and a mean free path on the order of 1 μm, which is the same order of magnitude as the arm length of our AB ring of $L \simeq 1.5$ μm. However, screening is reduced along the almost-depleted AB ring, such that the mean free path could be shorter. Hence, we conclude that the electron dynamics in our AB ring is located somewhere between the quasiballistic and the diffusive regime. One way to reach the ballistic regime in future devices will be to further reduce the intrinsic channel width such that quasi-one-dimensional channels can be realized at relatively large carrier densities. A further reduction of the screen-gate width by a factor of 4 is easily achievable by electron-beam lithography.

In Fig. 6(a), we present AB oscillations of the current $I - \bar{I}$ as a function of B and V_s, while in Fig. 6(b), we show an exemplary depletion curve plotting the current $\bar{I}(V_s)$ averaged over B. The latter strongly oscillates as observed for Coulomb-blockade oscillations, the current becomes small but stays finite in the Coulomb valleys. Such a behavior can be explained assuming two quantum dots in parallel [34], i.e., one dot in each arm of the AB ring, as indicated in the inset. The exact position of the quantum dots is thereby unknown. The overall resistance of $R \simeq 120\text{k}\Omega \gg h/e^2$ at the two distinct current maxima below $V_s - V_s^d = 10$ mV is in agreement with the assumption of two parallel dots giving rise to well-established Coulomb-blockade oscillations.

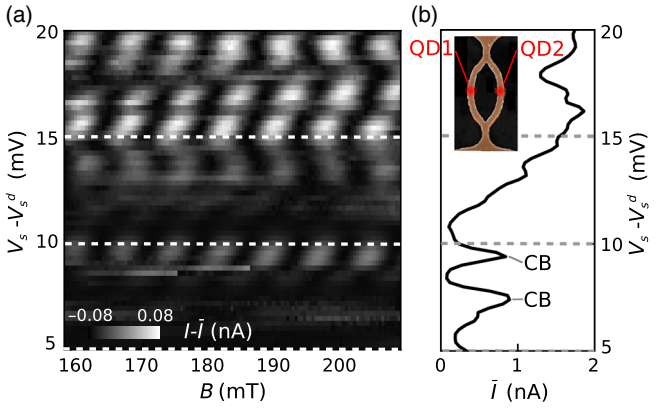

FIG. 6. (a) Current oscillations $I - \bar{I}$ as a function of the screen-gate voltage and the magnetic field at $V_t = -3$ V. The data shown in Fig. 5(a) are plots along the horizontal dashed lines. (b) Coulomb-blockade oscillations in $\bar{I}(V_s)$ (averaged over B). The inset displays an SEM image of the AB ring with possible positions of the two quantum dots indicated as QD1 and QD2. Two individual Coulomb-blockade maxima are indicated with CB. The bath temperature is $T = 25$ mK and the source-drain voltage $V = 0.1$ mV.

The two-terminal AB oscillations in Fig. 6(a) feature (i) continuous phase shifts at finite B values, confirming the contribution of multiple paths in each arm, and (ii) phase jumps as a function of V_s, confirming the existence of quantum dots in the arms of the AB ring (phase jumps were previously observed for one dot in one arm) [35,36]. Note that our ring is too small to explain the observed phase jumps by means of the electrostatic AB effect [32].

In the following, we discuss the dephasing as a function of temperature and source-drain voltage. In an ideal two-terminal AB ring composed of one-dimensional arm dephasing by energy broadening is absent at modest energies. The reason is phase rigidity [36–40] allowing only phase shifts by multiples of π, which would require either a very different arm length or an unreasonably large energy window. Such an ideal AB ring would be a perfect device to study the electron-electron interaction [41–43] remaining as a possible dephasing process. However, realistic AB rings such as ours host multiple paths compromising the phase rigidity, such that the temperature or source-drain voltage dependence of the dephasing at relatively small energies is dominated by energy broadening [44–47]. The measured temperature and source-drain voltage dependence of the visibility are presented in Fig. 7 for $V_s - V_s^d = 15$ mV, where the two-terminal resistance is $\simeq$60 kΩ; compare these results to Fig. 6(b). Having already established the existence of two parallel quantum dots,

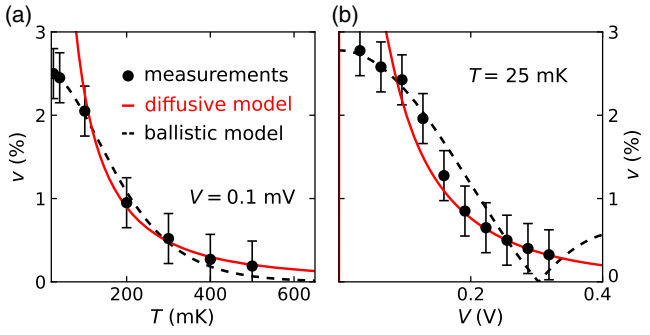

FIG. 7. Visibility (a) $v(T)$ at $V = 0.1$ mV and (b) $v(V)$ at $T = 25$ mK. $V_s - V_s^d = 15$ mV and $V_t = -3$ V. The solid red lines are model curves assuming diffusive transport calculated with (a) Eq. (2) and (b) Eq. (3) for $v_0 = 56\%$, $E_{\text{Th}} = 36$ μeV, $\alpha = 0.015$ ps meV$^{2/3}$, $\beta = 0.009$ ps meV$^{2/3}$, and $\kappa = 0.52$. Dashed black lines are calculated assuming ballistic transport with Eq. (4) for $v_0 = 2.56\%$, $\Delta\tau = 30$ ps, and $\kappa = 0.52$.

we now consider two scenarios, namely, either ballistic or diffusive transport between the quantum dots. Searching for an answer, we fit the measured data in Fig. 7 for two idealistic models. The first one assumes diffusive transport in an AB ring with quasi-one-dimensional arms for which the temperature dependence of the visibility has been obtained from the weak localization theory [48],

$$v(T) = v_0 \left(\frac{E_{\mathrm{Th}}}{k_B T}\right)^{1/2} \exp\left(\frac{-L}{\sqrt{D\tau_\phi}}\right), \tag{2}$$

with $\tau_\phi = \alpha(k_B T)^{-2/3}$ [49]. This equation takes into account thermal broadening (the square-root term) and decoherence by a scattering of electrons (the exponential term). Here, $E_{\mathrm{Th}} = \hbar D/L^2$ is the Thouless energy, D the 2D diffusion constant, and τ_ϕ the electrons' decoherence time. The according voltage dependence of the visibility derived from nonequilibrium dephasing models is [50,51]

$$v(V) = v_0 \left(\frac{e\kappa V}{E_{\mathrm{Th}}}\right)^{1/2} \exp\left(\frac{-L}{\sqrt{D\tau_\phi}}\right), \tag{3}$$

with $\tau_\phi = \beta(e\kappa V)^{-2/3}$ [52,53]. The prefactor $\kappa = 0.52$ takes into account the fact that part of the source-drain voltage V drops in the leads of the AB ring. The red solid lines in Fig. 7 are fits to the respective temperature and voltage dependences given by Eqs. (2) and (3). The diffusive model describes the measured data well for high energies but drastically overestimates the visibility at low T or V values. This deviation can be explained with the approximations done by assuming $V = 0$ for fitting the T dependence and $T = 0$ for fitting the V dependence. The actual fit parameters are listed in the caption of Fig. 7.

In our second idealistic scenario, we assume ballistic transport through the AB ring. Because the dwell time $\simeq L/v_F$ of an electron moving ballistically through the AB ring is short compared to τ_ϕ, in this case, we can neglect the influence of Nyquist noise, which leaves energy broadening as the only remaining dephasing process [49]. Combining voltage and temperature dependence at first order, the ballistic scenario can be described by [54]

$$v = 2\pi v_0 \frac{k_B T}{|e\kappa V|} \sinh^{-1}\left(\frac{\pi k_B T}{\hbar/\Delta\tau}\right) \left|\sin\left(\frac{e\kappa V}{2\hbar/\Delta\tau}\right)\right|, \tag{4}$$

where $\Delta\tau$ defines the difference of the dwell times of a ballistic electron in the two arms of the AB ring. A single fit to both data sets of Eq. (4) representing the ballistic model is shown as black dashed lines in Fig. 7. Our ballistic model describes the temperature dependence well but shows qualitative deviations in the voltage dependence (at high voltages). The actual fit parameters are listed in the caption of Fig. 7. We find a dwell-time difference of $\Delta\tau = 30$ ps. On the one hand, this corresponds to an unrealistically large arm-length difference of approximately 1 μm assuming ballistic motion at the Fermi velocity. On the other hand, the existence of a quantum dot in each arm leads to multiple reflections which would enhance dwell times. As a result, without further experimental and theoretical efforts, it is impossible to determine from our data whether transport through the AB ring is diffusive or ballistic. Diffusive transport might be caused by the almost complete depletion in the AB rings which is necessary to reduce the number of one-dimensional channels preventing a higher visibility. We believe that AB rings with narrower arms but higher carrier density will help to reach ballistic transport in the future and to reduce the chance of the formation of quantum dots.

V. CONCLUSION

In this article, we explore an alternative method to define mesoscopic circuits in heterostructures based on the electric-field effect. The idea is to deplete most of the 2DES by means of a global top gate. Only at those areas where carriers are needed are screen gates placed below the top gate used to shield the effect of the top gate locally. The resulting circuits are highly tunable on the nanoscale, as demonstrated in the presented experiments. Importantly, our method has the advantage of reducing the complexity of gate-defined nanostructures. In more detail, it provides a straightforward way to realize conducting paths with ring topology and offers a way to define complex structures with a smaller number of gates compared to the conventional technology based on multiple depletion gates. Our Aharonov-Bohm measurements demonstrate phase coherence comparable to that in conventional AB rings in semiconductors, which makes our method suitable for quantum-information applications. While not demonstrated here, the closer vicinity of a metal gate to the carriers is expected to lead to a reduction of the Coulomb interaction between carriers. As such, our method can be viewed as an alternative which will facilitate an increase in the variety of physical properties in nanocircuits. Future tasks will include the definition of quantum point contacts and chains of quantum dots by using screen gates.

ACKNOWLEDGMENTS

We thank P. Brouwer for the fruitful discussions and are grateful for the financial support from the DFG via Grant No. LU 819/4-1.

[1] R. E. Behringer, P. M. Mankiewich, and R. E. Howard, Fabrication of ultrahigh resolution structures in compound semiconductor heterostructures, J. Vac. Sci. Technol. B **5**, 326 (1987).

[2] K. Y. Lee, T. P. Smith III, C. J. B. Ford, W. Hansen, C. M. Knoedler, J. M. Hong, and D. P. Kern, Submicron trenching

of semiconductor nanostructures, Appl. Phys. Lett. **55**, 625 (1989).

[3] C. Ford, A. Fowler, J. Hong, C. Knoedler, S. Laux, J. Wainer, and S. Washburn, Gated, asymmetric rings as tunable electron interferometers, Surf. Sci. **229**, 307 (1990).

[4] E. A. Moon, J.-L. Lee, and H. M. Yoo, Selective wet etching of GaAs on $Al_xGa_{1-x}As$ for AlGaAs/InGaAs/AlGaAs pseudomorphic high electron mobility transistor, J. Appl. Phys. **84**, 3933 (1998).

[5] R. Held, T. Vancura, T. Heinzel, K. Ensslin, M. Holland, and W. Wegscheider, In-plane gates and nanostructures fabricated by direct oxidation of semiconductor heterostructures with an atomic force microscope, Appl. Phys. Lett. **73**, 262 (1998).

[6] T. Heinzel, R. Held, S. Lüscher, K. Ensslin, W. Wegscheider, and M. Bichler, Electronic properties of nanostructures defined in Ga[Al]As heterostructures by local oxidation, Physica (Amsterdam) **9E**, 84 (2001).

[7] A. D. Wieck and K. Ploog, In-plane-gated quantum wire transistor fabricated with directly written focused ion beams, Appl. Phys. Lett. **56**, 928 (1990).

[8] R. Held, S. Lüscher, T. Heinzel, K. Ensslin, and W. Wegscheider, Fabricating tunable semiconductor devices with an atomic force microscope, Appl. Phys. Lett. **75**, 1134 (1999).

[9] S. Platonov, B. Kästner, H. W. Schumacher, S. Kohler, and S. Ludwig, Lissajous Rocking Ratchet: Realization in a Semiconductor Quantum Dot, Phys. Rev. Lett. **115**, 106801 (2015).

[10] W. Walukiewicz, H. E. Ruda, J. Lagowski, and H. C. Gatos, Electron mobility in modulation-doped heterostructures, Phys. Rev. B **30**, 4571 (1984).

[11] S. W. Jung, T. Fujisawa, Y. Hirayama, and Y. H. Jeong, Background charge fluctuation in a GaAs quantum dot device, Appl. Phys. Lett. **85**, 768 (2004).

[12] C. Buizert, F. H. L. Koppens, M. Pioro-Ladrière, H.-P. Tranitz, I. T. Vink, S. Tarucha, W. Wegscheider, and L. M. K. Vandersypen, *In Situ* Reduction of Charge Noise in $GaAs/Al_xGa_{1-x}As$ Schottky-Gated Devices, Phys. Rev. Lett. **101**, 226603 (2008).

[13] D. Taubert, M. Pioro-Ladrière, D. Schröer, D. Harbusch, A. S. Sachrajda, and S. Ludwig, Telegraph Noise in Coupled Quantum Dot Circuits Induced by a Quantum Point Contact, Phys. Rev. Lett. **100**, 176805 (2008).

[14] D. Schröer, A. D. Greentree, L. Gaudreau, K. Eberl, L. C. L. Hollenberg, J. P. Kotthaus, and S. Ludwig, Electrostatically defined serial triple quantum dot charged with few electrons, Phys. Rev. B **76**, 075306 (2007).

[15] F. Forster, M. Mühlbacher, D. Schuh, W. Wegscheider, G. Giedke, and S. Ludwig, Multistability and spin diffusion enhanced lifetimes in dynamic nuclear polarization in a double quantum dot, Phys. Rev. B **92**, 245303 (2015).

[16] E. Buks, R. Schuster, M. Heiblum, D. Mahalu, and V. Umansky, Dephasing in electron interference by a "which-path" detector, Nature (London) **391**, 871 (1998).

[17] D.-I. Chang, G. L. Khym, K. Kang, Y. Chung, H.-J. Lee, M. Seo, M. Heiblum, D. Mahalu, and V. Umansky, Quantum mechanical complementarity probed in a closed-loop Aharonov-Bohm interferometer, Nat. Phys. **4**, 205 (2008).

[18] I. Zailer, J. E. F. Frost, V. Chabasseur-Molyneux, C. J. B. Ford, and M. Pepper, Crosslinked PMMA as a high-resolution negative resist for electron beam lithography and applications for physics of low-dimensional structures, Semicond. Sci. Technol. **11**, 1235 (1996).

[19] W. H. Teh and C. G. Smith, Fabrication of quasi-three-dimensional micro/nanomechanical components using electron beam cross-linked poly (methyl methacrylate) resist, J. Vac. Sci. Technol. B **21**, 3007 (2003).

[20] Below this structure follows a 650-nm-thick GaAs layer on top of 15 periods of a superlattice of 5-nm Al and 5-nm As to stick segregating impurities during the MBE growth at its interfaces and, thus, to keep the layers above clean. The 2DES is formed in the GaAs layer close to the interface of the $Al_{0.36}Ga_{0.64}As$ layer.

[21] A. Wieck and D. Reuter, in *Proceedings of the 26th International Symposium on Compound Semiconductors, Berlin, Germany, 1999* (Institute of Physics, Bristol, England, 2000), p. 51.

[22] C. J. B. Ford, T. J. Thornton, R. Newbury, M. Pepper, H. Ahmed, C. T. Foxon, J. J. Harris, and C. Roberts, The Aharonov-Bohm effect in electrostatically defined heterojunction rings, J. Phys. C **21**, L325 (1988).

[23] C. J. B. Ford, T. J. Thornton, R. Newbury, M. Pepper, H. Ahmed, D. C. Peacock, D. A. Ritchie, J. E. F. Frost, and G. A. C. Jones, Electrostatically defined heterojunction rings and the Aharonov-Bohm effect, Appl. Phys. Lett. **54**, 21 (1989).

[24] R. H. Harrell, K. S. Pyshkin, M. Y. Simmons, D. A. Ritchie, C. J. B. Ford, G. A. C. Jones, and M. Pepper, Fabrication of high-quality one- and two-dimensional electron gases in undoped GaAs/AlGaAs heterostructures, Appl. Phys. Lett. **74**, 2328 (1999).

[25] J. C. H. Chen, D. Q. Wang, O. Klochan, A. P. Micolich, K. D. Gupta, F. Sfigakis, D. A. Ritchie, D. Reuter, A. D. Wieck, and A. R. Hamilton, Fabrication and characterization of ambipolar devices on an undoped AlGaAs/GaAs heterostructure, Appl. Phys. Lett. **100**, 052101 (2012).

[26] A. Siddiki, J. Horas, D. Kupidura, W. Wegscheider, and S. Ludwig, Asymmetric nonlinear response of the quantized Hall effect, New J. Phys. **12**, 113011 (2010).

[27] S. Birner, T. Zibold, T. Andlauer, T. Kubis, M. Sabathil, A. Trellakis, and P. Vogl, NEXTNANO: General purpose 3-D simulations, IEEE Trans. Electron Devices **54**, 2137 (2007).

[28] G. A. Samara, Temperature and pressure dependences of the dielectric constants of semiconductors, Phys. Rev. B **27**, 3494 (1983).

[29] E. Ginossar, L. I. Glazman, T. Ojanen, F. von Oppen, W. E. Shanks, A. C. Bleszynski-Jayich, and J. G. E. Harris, Mesoscopic persistent currents in a strong magnetic field, Phys. Rev. B **81**, 155448 (2010).

[30] S. L. Ren, J. J. Heremans, C. K. Gaspe, S. Vijeyaragunathan, T. D. Mishima, and M. B. Santos, Aharonov-Bohm oscillations, quantum decoherence and amplitude modulation in mesoscopic InGaAs/InAlAs rings, J. Phys. Condens. Matter **25**, 435301 (2013).

[31] M. A. Castellanos-Beltran, D. Q. Ngo, W. E. Shanks, A. B. Jayich, and J. G. E. Harris, Measurement of the Full Distribution of Persistent Current in Normal-Metal Rings, Phys. Rev. Lett. **110**, 156801 (2013).

[32] W. G. van der Wiel, Y. V. Nazarov, S. De Franceschi, T. Fujisawa, J. M. Elzerman, E. W. G. M. Huizeling, S. Tarucha, and L. P. Kouwenhoven, Electromagnetic Aharonov-Bohm effect in a two-dimensional electron gas ring, Phys. Rev. B **67**, 033307 (2003).

[33] A. J. M. Giesbers, U. Zeitler, M. I. Katsnelson, D. Reuter, A. D. Wieck, G. Biasiol, L. Sorba, and J. C. Maan, Correlation-induced single-flux-quantum penetration in quantum rings, Nat. Phys. **6**, 173 (2010).

[34] R. P. Taylor, A. S. Sachrajda, P. Zawadzki, P. T. Coleridge, and J. A. Adams, Aharonov-Bohm Oscillations in the Coulomb Blockade Regime, Phys. Rev. Lett. **69**, 1989 (1992).

[35] M. Avinun-Kalish, M. Heiblum, O. Zarchin, D. Mahalu, and V. Umansky, Crossover from "mesoscopic" to "universal" phase for electron transmission in quantum dots, Nature (London) **436**, 529 (2005).

[36] A. Yacoby, R. Schuster, and M. Heiblum, Phase rigidity and $h/2e$ oscillations in a single-ring Aharonov-Bohm experiment, Phys. Rev. B **53**, 9583 (1996).

[37] L. Onsager, Reciprocal relations in irreversible processes. II., Phys. Rev. **38**, 2265 (1931).

[38] H. B. G. Casimir, On Onsager's principle of microscopic reversibility, Rev. Mod. Phys. **17**, 343 (1945).

[39] M. Buttiker, Symmetry of electrical conduction, IBM J. Res. Dev. **32**, 317 (1988).

[40] C. Kreisbeck, T. Kramer, S. S. Buchholz, S. F. Fischer, U. Kunze, D. Reuter, and A. D. Wieck, Phase shifts and phase π jumps in four-terminal waveguide Aharonov-Bohm interferometers, Phys. Rev. B **82**, 165329 (2010).

[41] S. Washburn, C. P. Umbach, R. B. Laibowitz, and R. A. Webb, Temperature dependence of the normal-metal Aharonov-Bohm effect, Phys. Rev. B **32**, 4789 (1985).

[42] S. Russo, J. B. Oostinga, D. Wehenkel, H. B. Heersche, S. S. Sobhani, L. M. K. Vandersypen, and A. F. Morpurgo, Observation of Aharonov-Bohm conductance oscillations in a graphene ring, Phys. Rev. B **77**, 085413 (2008).

[43] T. Capron, C. Texier, G. Montambaux, D. Mailly, A. D. Wieck, and L. Saminadayar, Ergodic versus diffusive decoherence in mesoscopic devices, Phys. Rev. B **87**, 041307 (2013).

[44] M. Cassé, Z. D. Kvon, G. M. Gusev, E. B. Olshanetskii, L. V. Litvin, A. V. Plotnikov, D. K. Maude, and J. C. Portal, Temperature dependence of the Aharonov-Bohm oscillations and the energy spectrum in a single-mode ballistic ring, Phys. Rev. B **62**, 2624 (2000).

[45] S. S. Buchholz, S. F. Fischer, U. Kunze, M. Bell, D. Reuter, and A. D. Wieck, Control of the transmission phase in an asymmetric four-terminal Aharonov-Bohm interferometer, Phys. Rev. B **82**, 045432 (2010).

[46] V. S.-W. Chung, P. Samuelsson, and M. Büttiker, Visibility of current and shot noise in electrical Mach-Zehnder and Hanbury Brown Twiss interferometers, Phys. Rev. B **72**, 125320 (2005).

[47] L. V. Litvin, H.-P. Tranitz, W. Wegscheider, and C. Strunk, Decoherence and single electron charging in an electronic Mach-Zehnder interferometer, Phys. Rev. B **75**, 033315 (2007).

[48] S. Washburn and R. A. Webb, Aharonov-Bohm effect in normal metal quantum coherence and transport, Adv. Phys. **35**, 375 (1986).

[49] M. Treiber, O. M. Yevtushenko, F. Marquardt, J. von Delft, and I. V. Lerner, Dimensional crossover of the dephasing time in disordered mesoscopic rings, Phys. Rev. B **80**, 201305 (2009).

[50] A. Larkin and D. E. Khmel'nitskii, Mesoscopic fluctuations of current-voltage characteristics, J. Exp. Theor. Phys. **64**, 1815 (1986).

[51] C. Terrier, D. Babić, C. Strunk, T. Nussbaumer, and C. Schönenberger, The amplitude of non-equilibrium quantum interference in metallic mesoscopic systems, Europhys. Lett. **59**, 437 (2002).

[52] A. B. Gougam, F. Pierre, H. Pothier, D. Esteve, and N. O. Birge, Comparison of energy and phase relaxation in metallic wires, J. Low Temp. Phys. **118**, 447 (2000).

[53] D. P. DiVincenzo and C. L. Kane, Voltage fluctuations in mesoscopic metal rings and wires, Phys. Rev. B **38**, 3006 (1988).

[54] K.-T. Lin, Y. Lin, C. C. Chi, J. C. Chen, T. Ueda, and S. Komiyama, Temperature- and current-dependent dephasing in an Aharonov-Bohm ring, Phys. Rev. B **81**, 035312 (2010).